Real-time autofocus of holograms based on image sharpness

Maxime Doury,[1,2] Nicolas Verrier,[1,2] Pierre Pagnoux,[1,2] Jeffrey Bencteux,[1,2] and Michael Atlan[1,2]

[1] *Ecole Supérieure de Physique et de Chimie Industrielles - ESPCI ParisTech, PSL Research University, Institut Langevin. 1 rue Jussieu, 75005, Paris, France*

[2] *Centre National de la Recherche Scientifique (CNRS) UMR 7587, Institut National de la Santé et de la Recherche Médicale (INSERM) U 979, Université Pierre et Marie Curie (UPMC), Université Paris Diderot. 1 rue Jussieu, 75005, Paris, France*

A comprehensive method for autofocus of optically-acquired holograms based on classical image features assessment is reported. The focus criterion relies on the image intensity, and the recorded optical phase is used for image rendering at a given distance. Focus seeking over a wide range of reconstruction distances is ensured by the continuity of the two holographic rendering algorithms used, which makes it suitable for both microscopic and macroscopic imaging. Calculations are performed on graphics processing units to enable versatile and robust real-time autofocus operation in experimental conditions.

OCIS codes : 090.0090, 090.1995.

I. INTRODUCTION

Various imaging and sensing applications benefit from the unconventional nature of holograms acquired by interferometry, enabling powerful features such as phase imaging of optical wavefronts, shot-noise sensitivity with traditional sensor arrays in low-light conditions, aperture synthesis, compressed sensing, and heterodyne detection. Some applications of this imaging scheme include microscopy [1–5], non-contact vibrometry [6–9], fluid dynamics metrology [10–14]. A powerful feature of optically-acquired holograms is to enable post-measurement refocus. Computational image rendering of complex-valued optical fields from holographic measurements can be performed by wave propagation algorithms. Classical methods used for numerical reconstruction rely on free-space propagation of the diffracted optical field in the Fresnel approximation. Nevertheless, manual focus procedures for image plane retrieval are still prevalent.

Classical image sharpness assessment methods are mostly based on the estimation of the variance, the gradient or the Laplacian of the spatial distribution of intensity [15–19]. Holographic interferometry can benefit from state-of-the-art focus metrics based on image sharpness criteria [20]. Optically-acquired interferograms need to be processed numerically to yield a hologram image, because of the specific nature of complex-valued diffracted optical field recordings. In contrast with direct imaging schemes, this digital treatment is performed after data acquisition in holography. Numerical image rendering is referred to as hologram refocusing. It was shown that at the focus distance, the amplitude of the hologram is minimum for a pure amplitude object and maximum for a pure phase object. Hence the amplitude of the reconstructed hologram can be used as a focus metric [4, 21–23]. The complex amplitude [24], the spectral content [25], sparsity metrics [26–28], the speckle pattern [29], axial variations [30] or the discrete cosine transform [31] of the hologram can also be used as sharpness metrics for the reconstruction of holograms. Furthermore, resampling of the holographic complex field has been proposed for fast focus assessment [32]. Focus criteria were also tested onto downsampled holograms to increase autofocus speed [33] while maintaining a stable global maximum in the sharpness curve. Focus metrics for color holograms were also proposed [4, 34]. The contrast of the rendered images affected by speckle was found to be a good focus metric, providing a single focus-value without ambiguity [35]. An active method, requiring the the use of structured illumination with a spatial light modulator was introduced for the microscopy of phase and amplitude objects [36].

In this paper, we report on a numerical autofocus method for optically-acquired digital holograms implemented on graphics processing units for real-time processing. After a definition of the discrete operators used for focus estimate computations, we will describe the two numerical optical field propagation methods used for hologram rendering, based on one and two fast Fourier transform (FFT) algorithms respectively. We will define their domains of validity and verify their continuity, in order to ensure that the autofocus method is valid over a wide range of reconstruction distances, and thus usable for both microscopic and macroscopic imaging. We will then define the focus criteria on the squared amplitude of the optical field we chose to combine for the proposed focus retrieval algorithm. The accuracy, robustness and versatility of this approach will be illustrated with experimental holograms.

II. DISCRETE OPERATORS USED FOR IMAGE RENDERING AND FOCUS RETRIEVAL

In digital holography, optical interferograms are recorded on a discrete sensor array. Therefore, the operators used in this article will be defined with their actual

discrete formulation. The proposed autofocus method is based on the estimation of the spatial features of images reconstructed by standard propagation algorithms. Most of the criteria used in this article to assess the best focus distance are based on bi-dimensional spatial convolution products calculations. According to the convolution theorem, the bi-dimensional spatial convolution of functions of discrete variable sequences x and K can the be written

$$x * K = \mathcal{F}^{-1}\{\mathcal{F}\{x\} \times \mathcal{F}\{K\}\} \tag{1}$$

The 2D fast Fourier transform of an array x is noted $\mathcal{F}\{x\}$, and the 2D inverse fast Fourier transform of x is $\mathcal{F}^{-1}\{x\}$. The kernel K is zero-padded to the size of the array x, to ensure size matching of both arrays, in practice. The operator $\times$ denotes the multiplication of matching array elements. One can finally define the averaging operator $\langle . \rangle$ by $\langle x \rangle = (MN)^{-1} \sum_{m=1}^{M} \sum_{n=1}^{N} x_{m,n}$

III. HOLOGRAM RECONSTRUCTION

A. Introduction

Typical hologram acquisition schemes involve interferometric techniques [37–43]. Under spatial and/or temporal modulation of the recorded interference pattern, one can retrieve the spatial distribution in the sensor plane of the complex optical field E diffracted by the object (Fig. 1). The magnitude and the phase of the digitized object wave, assessed at each pixel of a sensor array of $M \times N$ pixels of pitch $d_x = d_y = d$, is indexed by the integers (m, n). The complex-valued discrete scalar field $E(x, y, z) = \{E_{m,n}(z)\} \equiv E(z)$ in the plane z is the field's dimensionless magnitude. The intensity of the optical field in the plane z is computed as

$$I(z) = |E(z)|^2 \tag{2}$$

Holograms can be rendered numerically via the use of scalar diffraction theories. Several methods can be considered for hologram reconstruction [44–52]. In this article, we make use of the Fourier approach (one-FFT algorithm) and the angular spectrum propagation approach (two-FFT algorithm) for the computation of the propagation integral of the optical field.

B. Propagation integrals of the optical field

Provided only small angles are involved during the propagation process, under paraxial conditions, the optical field E at point (x, y, z) is given with good accuracy by the Fresnel diffraction integral [53, 54]

$$E(x, y, z) \approx \frac{e^{ikz}}{i\lambda z} \iint E(x', y', 0) \times \exp\left[\frac{ik}{2z}\left((x - x')^2 + (y - y')^2\right)\right] \mathrm{d}x'\mathrm{d}y' \tag{3}$$

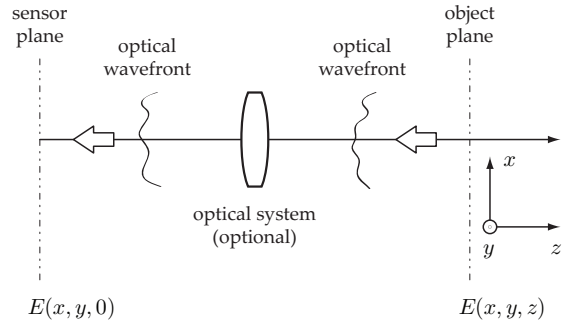

FIG. 1. Optical configuration. The optical radiation field E propagates along the optical axis z from the object plane to the sensor plane in free space; an optical system can be present. The diffracted field is recorded in the plane $z = 0$.

where λ is the wavelength and $k = 2\pi/\lambda$ is the wavenumber of the optical wave. For large diffraction angles, the propagation of the angular spectrum $\hat{E}(k_x, k_y, z) = \hat{E}(k_x, k_y, 0) \exp(ik_z z)$ of the field's distribution $E(x, y, z)$, yields to another diffraction integral [53, 54]

$$E(x, y, z) \approx \iint \hat{E}(k_x, k_y, 0) \times \exp(ik_z z) \exp(ik_x x + ik_y y) \, \mathrm{d}k_x \mathrm{d}k_y \tag{4}$$

where $\hat{E}(k_x, k_y, 0)$ is the two-dimensional Fourier transform of the field $E(x, y, 0)$, and $k_z = \sqrt{k^2 - k_x^2 - k_y^2}$ is the wavevector projection along z.

C. One-FFT rendering algorithm

Under the paraxial approximation, the discrete form of the propagation integral of the optical field can be written as [53]

$$E(z) = \mathcal{F}\{E(z = 0) \times h(z)\} \tag{5}$$

where $h(z) = \{h_{m,n}(z)\}$ is free-space propagation impulse response

$$h_{m,n}(z) = \frac{1}{i\lambda z} \exp\left[\frac{2i\pi z}{\lambda} + \frac{i\pi}{\lambda z}(m^2 d^2 + n^2 d^2)\right] \tag{6}$$

Here, $z = 0$ is associated with the sensor plane, and z corresponds to the object plane. For optimal reconstruction, the distance parameter z has to be accurately determined. As discussed further, the one-FFT rendering method will be suited for reconstruction of holograms of extended objects located far from the sensor (*i.e.* macroscopic imaging). The pitch Δx_1 of the reconstructed hologram (Fig. 2) can be derived geometrically from the ratio of the angular acceptance $\sim \lambda/d$ of one pixel behaving as a heterodyne antenna [55], the number of pixels

of the receiver in the considered direction N, and the reconstruction distance z.

$$\Delta x_1(z) = \frac{\lambda z}{Nd} \tag{7}$$

Hence the discrete lateral coordinates of a hologram rendered with the one-FFT algorithm are $(x, y) = (m\Delta x, n\Delta y)$. The lateral field of view scales up linearly with z (Fig. 2).

D. Two-FFT rendering algorithm

The propagation integral of the optical field can also be viewed as the propagation of its angular spectrum, and can be expressed as a spatial convolution product [53]

$$E(z) = \mathcal{F}^{-1}\{\mathcal{F}\{E(z=0)\} \times H(z)\} \tag{8}$$

where $H(z) = \{H_{m,n}(z)\}$ is the angular spectrum propagation kernel defined as

$$H_{m,n}(z) = \exp\left[\frac{2i\pi z}{\lambda}\sqrt{1-\left(\frac{m\lambda}{Md}\right)^2-\left(\frac{n\lambda}{Nd}\right)^2}\right] \tag{9}$$

The function $H(z)$ is the Fourier transform of the free-space impulse response h (Eq. 6). The angular spectrum propagation will have to be used as a reconstruction method when dealing with small objects located near the sensor (*i.e.* microscopic imaging). With two-FFT rendering, the pitch Δx_2 of the reconstructed hologram does not depend on the reconstruction distance (Fig. 2). It is equal to the pitch in the sensor plane

$$\Delta x_2 = d \tag{10}$$

In order to make the proposed autofocus procedure versatile and applicable for both macroscopic and microscopic imaging, the switching conditions from one formalism to the other are now investigated.

E. Hologram rendering method versus reconstruction distance

To ensure an effective autofocus procedure for both macroscopic and microscopic holographic imaging, the influence of the parameter z on spatial sampling of the kernels defined in Eq. 6 and Eq. 9 was investigated. For accurate sampling, the argument of the exponent in the right member of equation Eq. 6 has to be assessed at reconstruction distances z satisfying [56–58]

$$z \geq \frac{Nd^2}{\lambda} = z_b \tag{11}$$

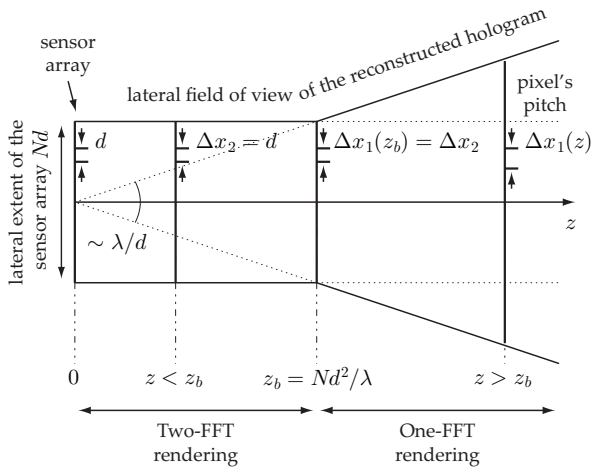

FIG. 2. Pixel's pitch Δx and lateral field of view $M\Delta x$ versus reconstruction distance z, in the case of free-space propagation.

The boundary value z_b of the reconstruction distance parameter is determined by equaling the highest spatial frequency of the quadratic phase in the exponent of Eq. 6 with the Nyquist frequency $(Nd)^{-1}$. In the same manner, according to the Nyquist-Shannon sampling theorem, the argument of the exponent in the right member of equation Eq. 9 has to be calculated at reconstruction distances z satisfying

$$z \leq z_b \tag{12}$$

For the value z_b of the parameter z, image pitches of both reconstruction methods are equal

$$\Delta x_1(z_b) = \Delta x_2 \tag{13}$$

Hence, a piecewise continuous rendering method valid for all values of the reconstruction parameter $z \in \mathbb{R}$ has been defined. The reconstruction distance z_b is the boundary value of the parameter z at which image rendering is switched between one-FFT (Eq. 5) and two-FFT algorithms (Eq. 8).

IV. SELECTED FOCUS CRITERIA

A focus function processes an image and condenses its in-focus estimate into a scalar value. The basic assumption on which are based most of these functions is that well-focused images contain more information and details than unfocused images [59], consequently they contain more high spatial frequency information, are more contrasted and their edges are sharper than for defocused images. A good immunity to noise is also a requirement for a focus function as it permits the use of the algorithm under real conditions. In addition to its immunity to noise, the ideal focus function response should

be unique, accurate and sharp. The reconstruction distance given by the focus function maximum and the actual object-sensor distance should be as close as possible. The presence of an irrelevant maximum can trap the autofocus algorithm, thus the number of local maxima should be as low as possible. Finally, the sharper the response is, the more precisely the focus distance can be determined. The proposed focus metric uses three classical focus criteria based on the spatial features of the reconstructed holograms : the global variance of the intensity, the average local variance of the intensity, and the average magnitude of the intensity gradient.

A. Global variance of the intensity

The global variance evaluates the non-normalized contrast of the image and characterizes its focusing as it measures the variations among the pixels of the image. Bright and dark pixels have the same influence. The global spatial variance of the intensity is defined as

$$V\{I\} = \langle (I - \langle I \rangle)^2 \rangle \tag{14}$$

where $\langle . \rangle$ is the spatial averaging operator.

B. Average local variance of the intensity

The local variance characterizes the local sharpness of image features. The local variance at pixel (m, n) in the neighborhood delimited by the extent of the kernel K_E, used for its computation in reciprocal space, is noted $V_L\{I\}_{m,n}$. Its average value over the reconstructed image I is

$$\langle V_L\{I\} \rangle = \left\langle (I - I * K_E)^2 \right\rangle \tag{15}$$

where the kernel K_E is a made of a 3×3 matrix of ones

$$K_E = \frac{1}{9} \begin{bmatrix} 1 & 1 & 1 \\ 1 & 1 & 1 \\ 1 & 1 & 1 \end{bmatrix} \tag{16}$$

C. Average magnitude of the intensity gradient computed by the Sobel operator

The Sobel operator is a discrete differentiation operator that computes an approximation of the image gradient [60, 61]. For each pixel, it outputs a bidimensional vector that contains the value of the spatial derivatives in the horizontal and vertical directions. A large magnitude reveals a sharp edge in the direction pointed by the vector. The average value of the Sobel gradient's magnitude on the intensity image I is defined as

$$\langle \|S\{I\}\| \rangle = \left\langle \left[(I * K_S)^2 + \left(I * K_S^T\right)^2 \right]^{1/2} \right\rangle \tag{17}$$

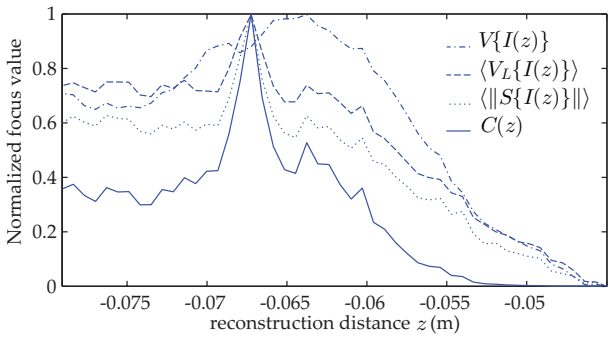

FIG. 3. Focus criteria versus reconstruction distance parameter z. The refocused hologram is shown in Fig. 7.

where the convolution products $I * K_S$ and $I * K_S^T$ are the directional gradients. The matrix K_S^T is the transpose of the matrix K_S. The Sobel kernel K_S is defined as

$$K_S = \begin{bmatrix} 1 & 0 & -1 \\ 2 & 0 & -2 \\ 1 & 0 & -1 \end{bmatrix} \tag{18}$$

V. COMPOUND FOCUS METRIC

Our choice of focus metric was guided by the need to comply with a a broad range of experimental conditions. To avoid a case-specific approach, we selected three classical focus criteria of intensity images calculated by Eq. 2. Four objects were studied in various recording conditions, as reported in Fig. 5, Fig. 4, Fig.6, and Fig. 7). The chosen focus metric combines the assessment of the global variance of the intensity (Eq. 14), the average local variance of the intensity (Eq. 15), and the average magnitude of the intensity gradient (Eq. 17). The focus metric $C(z)$ is the product of these three criteria

$$C(z) = V\{I(z)\} \times \langle V_L\{I(z)\} \rangle \times \langle \|S\{I(z)\}\| \rangle \tag{19}$$

To demonstrate the versatility and robustness, we applied the proposed autofocus method to the reconstruction of various experimental holograms acquired in macroscopic and microscopic imaging conditions.

A. Autofocus of macroscopic images

Holographic interferometry is widely used in vibration imaging [9, 63–69]. For accurate vibration pattern mapping, the assessment of the reconstruction distance is important. Our approach has two steps. First, a coarse logarithmic sweep is performed on a wide range of reconstruction distances, from $z = -5$ m to $z = 5$ m, leading to an estimation of the refocusing distance. Then, a fine linear sweep is realized around the distance z for which a maximum of $C(z)$ was found during the coarse sweep.

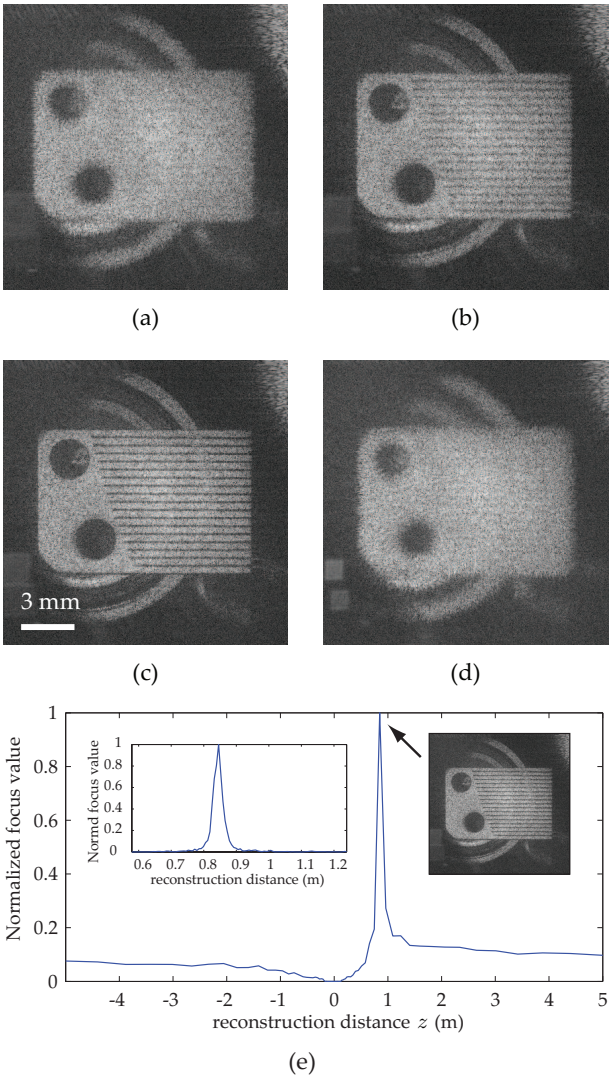

FIG. 4. Image rendering of the lamellophone of a musical box [62]. Intensity holograms reconstructed for distance parameters $z = 0.75\,\mathrm{m}$ (a), $z = 0.81\,\mathrm{m}$ (b), $z = 0.845\,\mathrm{m}$ (c), $z = 1\,\mathrm{m}$ (d). Image (c) was calculated for the maximum of $C(z)$. (Media 1)

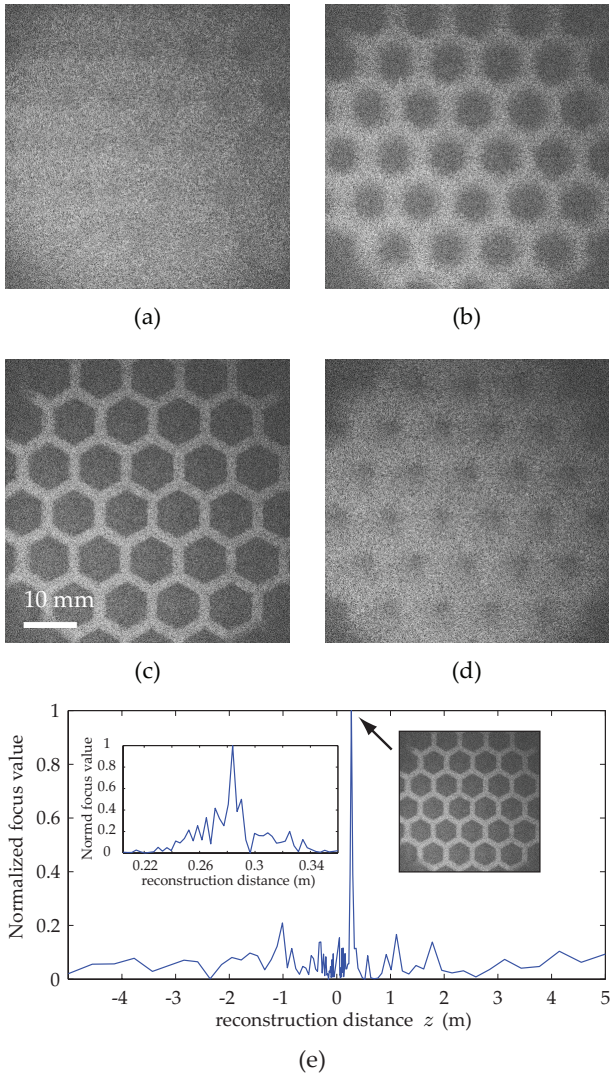

FIG. 5. Image rendering of a thin metallic plate with hexagonal holes [70]. Intensity holograms reconstructed for distance parameters $z = 0.22\,\mathrm{m}$ (a), $z = 0.26\,\mathrm{m}$ (b), $z = 0.28\,\mathrm{m}$ (c), $z = 0.35\,\mathrm{m}$ (d). Image (c) was calculated for the maximum of $C(z)$. (Media 2)

It should be noted that the ability of the proposed algorithm to operate at any reconstruction distance z is ensured by the switching condition at $z = z_b$ from Eq. 11 to Eq. 12. Results obtained for the image of the metallic lamellophone of a musical box [62] are reported in Fig. 4. Here the values of the focus metric $C(z)$ are plotted against z for both coarse and fine (inset) sweeps of the reconstruction distance. Reconstructed images, around the maximum of the fine sweep curve, corresponding to out-of-focus (Fig. 4(a), (b), and (d)) and in-focus holograms (Fig. 4(c)) attest of the sensitivity of the proposed algorithm. The same focus procedure was also applied to the hologram of a thin metallic plate carved with periodic hexagonal holes, used for vibrometry purposes [70]. Performing a coarse logarithmic sweep followed by a fine linear sweep makes it possible to bring the acquired hologram back to focus accurately, as reported in Fig. 5.

B. Autofocus of laser Doppler blood flow images

Holographic detection enables characterization of biological samples in-vivo [1, 2, 72, 73]. In particular, it provides a convenient way to perform wide-field optical heterodyne detection with a sensor array at video frame rate. Time-averaged holography with a frequency-shifted reference beam permits narrow band detection and imaging of local Doppler broadenings at low radiofrequencies. With this approach, blood flow contrasts can be imaged in the cerebral cortex [71] and in the eye fundus [74] of ro-

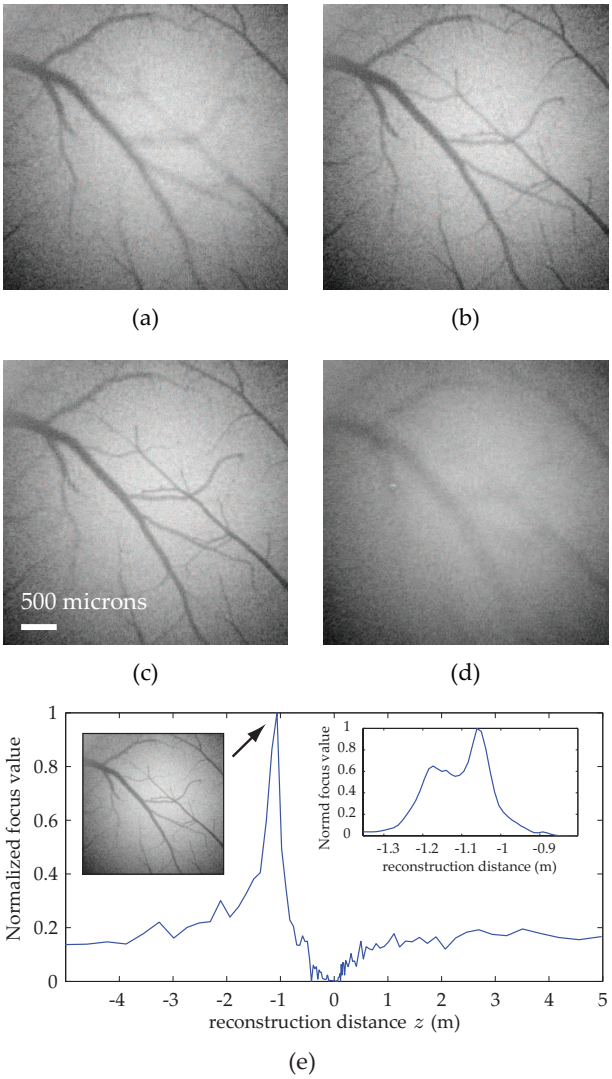

FIG. 6. Image rendering of the cerebral cortex of a mouse, acquired by laser Doppler holography [71]. Intensity holograms reconstructed for distance parameters $z = -1.5\,\mathrm{m}$ (a), $z = -1.2\,\mathrm{m}$ (b), $z = -1.055\,\mathrm{m}$ (c), $z = -0.7\,\mathrm{m}$ (d). Image (c) was calculated for the maximum of $C(z)$. (Media 3)

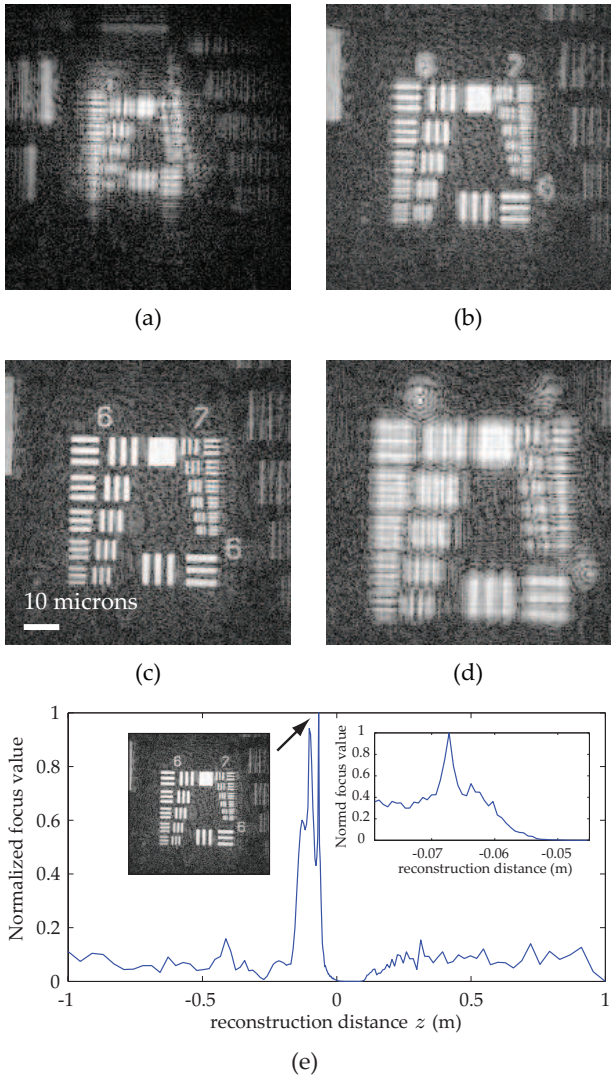

FIG. 7. Image rendering of a negative resolution target observed by holographic microscopy [50]. Intensity holograms reconstructed for distance parameters $z = -0.08\,\mathrm{m}$ (a), $z = -0.07\,\mathrm{m}$ (b), $z = -0.0677\,\mathrm{m}$ (c), $z = -0.06\,\mathrm{m}$ (d). Image (c) was calculated for the maximum of $C(z)$. (Media 4)

dents with a standard camera. The autofocus procedure was performed on the recording of a rodent's cerebral cortex, in vivo. The two-step sweep procedure was used to assess the maximum of the focus function $C\,(z)$ on the Doppler hologram of the living tissue to estimate the refocus distance (Fig. 6). A coarse logarithmic sweep from $z = -5$ m to $z = 5$ m, leads to a first estimate of the refocusing distance of $z \simeq -1.1\,\mathrm{m}$. Then, a fine linear sweep is realized around this value. The image of the vessels at the surface of the cerebral cortex is accurately refocused at the maximum of the focus function $C(z)$.

C. Autofocus of microscopic images

Microscopic imaging benefits from the three-dimensional content of digital holography [75–78]. However precise refocusing of the investigated objects remains a tedious task. The proposed autofocus procedure was tested in microscopic imaging conditions. Image acquisition of a resolution target was performed in heterodyne holographic microscopy configuration [5, 79, 80]. As for macroscopic imaging, a two-step sweep of the focus distance is performed to estimate the best reconstruction distance (Fig. 7(e)). Values of the focus metric $C\,(z)$ are plotted against the reconstruction distance z for both coarse and fine (inset) sweep attest for the applicability of the presented

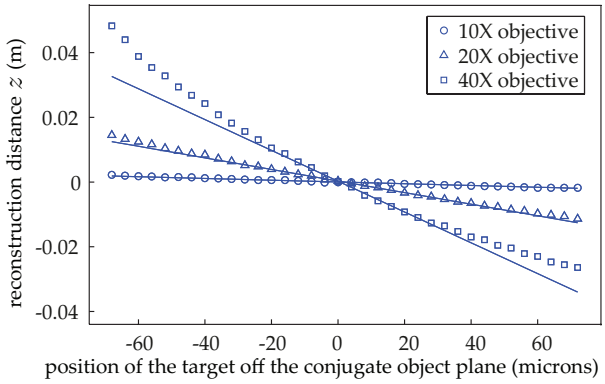

FIG. 8. Reconstruction distance versus position from the conjugate object plane, for three microscope objectives : 10× (NA .25), 20× (NA .40), 40× (NA .63).

scheme to holographic microscopy with a coherent light source. These results are confirmed by the focus images, depicted Fig. 7(a-d). The accuracy of focus distance retrieval is reported in Fig. 8. Actual positions of the target with respect to the focal plane are plotted against the reconstruction distance. For three microscope objectives with the following magnification factors and numerical apertures (NA) : 10× (NA .25), 20× (NA .40), 40× (NA .63), holograms for object positions ranging from -80 μm to 80 μm from the conjugate object plane are acquired. For each hologram, the proposed autofocus procedure is applied, leading to the evaluation of the estimated distance against the actual object position with respect to the focal plane reported in Fig. 8. The experimental results obtained with 10× (dots), 20× (circles), and 40× (crosses) objectives are superimposed with linear fits. The nominal magnification of microscope objectives is only achievable when the object is positioned in the object focal plane of the objective, and when the imaging sensor is positioned at the end of the microscope objective tube (at the image focal plane of the tube lens for infinity corrected microscope objectives). Within these conditions, the microscope objective works in optimal imaging conditions in terms of aberration correction. When these conditions are not fulfilled, magnification will both depend on the object-to-focal plane distance, and on the sensor-to-best correction plane of the microscope objective. In that case, the relationship between the actual object position and retrieved object position will not be linear. This effect is clearly noticeable in Fig. 8 for the 40× objective. Both the 10×, and 20× objective will exhibit the same behavior, however due to their smaller numerical aperture that affects their depth of field, this effect will appear at higher reconstruction distances.

VI. CONCLUSION

In conclusion, we have demonstrated a real-time autofocus procedure for holographic image rendering. Our approach is based on the analysis of spatial features of reconstructed intensity holograms. The retained focus method is the compound of three selected contrast criteria chosen for their versatility, allowing several imaging applications, and their compliance with long-distance and short-distance image rendering methods, with one- and two-FFT rendering algorithms, respectively. The continuity at both rendering methods' boundaries was investigated and used to enable focus retrieval at any reconstruction distance. Focus criteria were expressed in terms of discrete spatial convolutions and computed via discrete Fourier transforms. The proposed focus criterion was shown to enable robust and unique renderings when applied to various recording conditions. The accuracy of the method was validated over several detection configurations and a wide range of reconstruction distances. The proposed focus metric for holographic imaging of intensity images is versatile and robust. However, though focus planes are accurately found in the case of macroscopic and microscopic imaging, the retrieved reconstruction distance does not always match the real object position. This can usually happen because (i) a lens in the object channel is present, and (ii) the reference beam's wavefront is not perfectly flat in the sensor plane : the effective curvature of the measured field results from the difference between the object and the reference wavefronts. Therefore, the relation between the reconstruction distance and the physical object position might be calibrated for quantitative focus distance measurements.

ACKNOWLEDGMENTS

We gratefully acknowledge financial support from Agence Nationale de la Recherche (ANR-09-JCJC-0113, ANR-11-EMMA-046), Fondation Pierre-Gilles de Gennes (FPGG014), région Ile-de-France (C'Nano, AIMA), the Investments for the Future program (LabEx WIFI: ANR-10-LABX-24, ANR-10-IDEX-0001-02 PSL*), and European Research Council (ERC Synergy HELMHOLTZ).

[1] F. Charriére, N. Pavillon, T. Colomb, C. Depeursinge, T.J. Heger, E.A.D Mitchell, P. Marquet, and B. Rappaz. Living specimen tomography by digital holographic microscopy: morphometry of testate amoeba. *Opt. Express*, 14:7005–7013, 2006.

[2] B. Kemper and G. von Bally. Digital holographic microscopy for live cell application and technical inspection. *Appl. Opt.*, 47:A52–A61, 2008.

[3] Myung K Kim. Principles and techniques of digital holographic microscopy. *Journal of Photonics for Energy*,

pages 018005–018005, 2010.

[4] Jérôme Dohet-Eraly, Catherine Yourassowsky, and Frank Dubois. Refocusing based on amplitude analysis in color digital holographic microscopy. *Opt. Lett.*, 39(5):1109–1112, Mar 2014.

[5] F. Verpillat, F. Joud, P. Desbiolles, and M. Gross. Dark-field digital holographic microscopy for 3d-tracking of gold nanoparticles. *Opt. Express*, 19(27):26044–26055, Dec 2011.

[6] P. Picart, J. Leval, D. Mounier, and S. Gougeon. Some opportunities for vibration analysis with time averaging in digital fresnel holography. *Applied Optics*, 44(3):337–343, 2005.

[7] J. Leval, P. Picart, J.P. Boileau, and Pascal J.C. Full-field vibrometry with digital fresnel holography. *Appl. Opt.*, 44:5763–5772, 2005.

[8] V.R. Asundi, A. Singh. Time-averaged in-line digital holographic interferometry for vibration analysis. *Appl. Opt.*, 45:2391–2395, 2006.

[9] F. Joud, F. Laloë, M. Atlan, J. Hare, and M. Gross. Imaging a vibrating object by sideband digital holography. *Opt. Express*, 17(4):2774–2779, 2009.

[10] F. Dubois, N. Callens, C. Yourassowsky, M. Hoyos, P. Kurowski, and O. Monnom. Digital holographic microscopy with reduced spatial coherence for three-dimensional particle flow analysis. *Applied Optics*, 45(5):864–871, 2006.

[11] M. Atlan and M. Gross. Laser doppler imaging, revisited. *Review of Scientific Instruments*, 77(11):1161031–1161034, 2006.

[12] J.M. Desse, P. Picart, and P. Tankam. Digital three-color holographic interferometry for flow analysis. *Opt. Express*, 16:5471–5480, 2008.

[13] N. Verrier, S. Coetmellec, M. Brunel, and D. Lebrun. Digital in-line holography in thick optical systems: application to visualization in pipes. *Appl. Opt.*, 47:4147–4157, 2008.

[14] S Andrew Wormald and Jeremy M Coupland. On measuring 3d flow within inkjet droplet streams using a digital holographic microscope. *Journal of Modern Optics*, 57(9):700–708, 2010.

[15] Frans CA Groen, Ian T Young, and Guido Ligthart. A comparison of different focus functions for use in autofocus algorithms. *Cytometry*, 6(2):81–91, 1985.

[16] A. Santos, C. Ortiz de Solórzano, J.J. Vaquero, J.M. Pena, N. Malpica, and F. Del Pozo. Evaluation of autofocus functions in molecular cytogenetic analysis. *J. Microscopy*, 188:264–272, 1997.

[17] Jan-Mark Geusebroek, Frans Cornelissen, Arnold WM Smeulders, and Hugo Geerts. Robust autofocusing in microscopy. *Cytometry*, 39(1):1–9, 2000.

[18] Y. Sun, S. Duthaler, and B.J. Nelson. Autofocusing in computer microscopy: selecting the optimal focus algorithm. *Microscopy Research and Technique*, 65:139–149, 2004.

[19] Feimo Shen, Louis Hodgson, Jeffrey H Price, and Klaus M Hahn. Digital differential interference contrast autofocus for high-resolution oil-immersion microscopy. *Cytometry Part A*, 73(7):658–666, 2008.

[20] Hazar A İlhan, Mert Doğar, and Meriç Özcan. Digital holographic microscopy and focusing methods based on image sharpness. *Journal ofMicroscopy*, 2014.

[21] F. Dubois, C. Schockaert, N. Callens, and C. Yourassowsky. Focus plane detection criteria in digital holography microscopy by amplitude analysis. *Optics Express*, 14(13):5895–5908, 2006.

[22] A. El Mallahi and F. Dubois. Dependency and precision of the refocusing criterion based on amplitude analysis in digital holographic microscopy. *Opt. Express*, 19:6684–6698, 2011.

[23] Frank Dubois, Ahmed El Mallahi, Jérôme Dohet-Eraly, and Catherine Yourassowsky. Refocus criterion for both phase and amplitude objects in digital holographic microscopy. *Optics letters*, 39(15):4286–4289, 2014.

[24] G. Pan and H Meng. Digital holography of particle fields: reconstruction by use of complex amplitude. *Appl. Opt.*, 42:827–833, 2003.

[25] W. Li, N.C Loomis, Q. Hu, and C.S. Davis. Focus detection from digital in-line holograms based on spectral l_1 norms. *J. Opt. Soc. Am. A*, 24:3054–3062, 2007.

[26] M. Liebling and M. Unser. Autofocus for digital fresnel holograms by use of a fresnelet-sparsity criterion. *J. Opt. Soc. Am. A*, 21:2424–2430, 2004.

[27] Pasquale Memmolo, Melania Paturzo, Bahram Javidi, Paolo A Netti, and Pietro Ferraro. Refocusing criterion via sparsity measurements in digital holography. *Optics Letters*, 39(16):4719–4722, 2014.

[28] Xin Fan, John J Healy, and Bryan M Hennelly. Investigation of sparsity metrics for autofocusing in digital holographic microscopy. *Optical Engineering*, 56(5):053112–053112, 2017.

[29] Juanjuan Zheng, Giancarlo Pedrini, Peng Gao, Baoli Yao, and Wolfgang Osten. Autofocusing and resolution enhancement in digital holographic microscopy by using speckle-illumination. *Journal of Optics*, 17(8):085301, 2015.

[30] Meng Lv, Dayan Li, and Guohai Situ. Autofocus in digital holography by the first order longitudinal difference. In *Digital Holography and Three-Dimensional Imaging*, pages DW5E–9. Optical Society of America, 2016.

[31] Wen-Bo Cao, Ping Su, Jian-She Ma, and Xian-Ting Liang. A method for detecting the best reconstructing distance in phase-shifting digital holography. *Optics Communications*, 2014.

[32] M. Fatih Toy, J. Kühn, S. Richard, J. Parent, M. Egli, and C. Depeursinge. Accelerated autofocusing of off-axis holograms using critical sampling. *Opt. Lett.*, 37:5094–5096, 2012.

[33] Hazar A İlhan, Mert Doğar, and Meriç Özcan. Fast autofocusing in digital holography using scaled holograms. *Optics Communications*, 287:81–84, 2013.

[34] Peng Gao, Baoli Yao, Romano Rupp, Junwei Min, Rongli Guo, Baiheng Ma, Juanjuan Zheng, Ming Lei, Shaohui Yan, Dan Dan, and Tong Ye. Autofocusing based on wavelength dependence of diffraction in two-wavelength digital holographic microscopy. *Opt. Lett.*, 37(7):1172–1174, Apr 2012.

[35] P. Memmolo, C. Distante, M. Paturzo, A. Finizio, P. Ferraro, and B. Javidi. Automatic focusing in digital holography and its application to stretched holograms. *Opt. Lett.*, 36:1945–1947, 2011.

[36] Peng Gao, Giancarlo Pedrini, and Wolfgang Osten. Structured illumination for resolution enhancement and autofocusing in digital holographic microscopy. *Opt. Lett.*, 38(8):1328–1330, Apr 2013.

[37] D. Gabor. A new microscopic principle. *Nature*, 161:777–778, 1948.

[38] Gordon L Rogers. Xiv.—experiments in diffraction microscopy. *Proceedings of the Royal Society of Edinburgh. Section A. Mathematical and Physical Sciences*, 63(03):193–221, 1952.

[39] Yu N Denisyuk. Photographic reconstruction of the optical properties of an object in its own scattered radiation field. In *Soviet Physics Doklady*, volume 7, page 543, 1962.

[40] E.N. Leith and J. Upatnieks. Reconstructed wavefronts and communication theory. *JOSA*, 52(10):1123–1128, 1962.

[41] George W. Stroke. Lensless fourier-transform method for optical holography. *Applied Physics Letters*, 6(10):201–203, 1965.

[42] S. Guel-Sandoval and J. Ojeda-Casta neda. Quasi-fourier transform of an object from a fresnel hologram. *Appl. Opt.*, 18(7):950–951, Apr 1979.

[43] Ichirou Yamaguchi and Tong Zhang. Phase-shifting digital holography. *Opt. Lett.*, 22(16):1268–1270, Aug 1997.

[44] U. Schnars and W. Juptner. Direct recording of holograms by a ccd target and numerical reconstruction. *Appl. Opt.*, 33:179–181, 1994.

[45] U. Schnars and W. P. O. Juptner. Digital recording and numerical reconstruction of holograms. *Meas. Sci. Technol.*, 13:R85–R101, 2002.

[46] Myung K Kim, Lingfeng Yu, and Christopher J Mann. Interference techniques in digital holography. *Journal of Optics A: Pure and Applied Optics*, 8(7):S518–S523, 2006.

[47] J. Li, P. Tankam, Z. Peng, and P. Picart. Digital holographic reconstruction of large object using a convolution approach and adjustable magnification. *Opt. Lett.*, 34:572–574, 2009.

[48] J. F. Restrepo and J. Garcia-Sucerquia. Magnified reconstruction of digitally recorded holograms by fresnel-bluestein transform. *Appl. Opt.*, 49:6430–6435, 2010.

[49] Changgeng Liu, Dayong Wang, John J. Healy, Bryan M. Hennelly, John T. Sheridan, and Myung K. Kim. Digital computation of the complex linear canonical transform. *J. Opt. Soc. Am. A*, 28(7):1379–1386, Jul 2011.

[50] Nicolas Verrier and Michael Atlan. Off-axis digital hologram reconstruction: some practical considerations. *Appl. Opt.*, 50(34):H136–H146, Dec 2011.

[51] D.P. Kelly and D. Claus. The filtering role of the sensor pixel in fourier and fresnel digital holography. *Appl. Opt.*, 2012.

[52] Georges Nehmetallah and Partha P. Banerjee. Applications of digital and analog holography in three-dimensional imaging. *Adv. Opt. Photon.*, 4(4):472–553, Dec 2012.

[53] J.W. Goodman. *Introduction to Fourier Optics*. Roberts & Company Publishers, 2005.

[54] M. Born and E. Wolf. *Principles of Optics*. Cambridge Univ. Press, 1999.

[55] A.E. Siegman. The antenna properties of optical heterodyne receivers. *Applied Optics*, 5(10):1588, 1966.

[56] T. Kreis. *Handbook of Holographic Interferometry, Optical and Digital Methods*. Wiley-VCH, 2005.

[57] Y. Zhang, G. Shen, A. Schröder, and J. Kompenhans. Influence of some recording parameters on digital holographic particle image velocimetry. *Opt. Eng.*, 45:075801, 2006.

[58] D. Lebrun, D. Allano, L. Méès, F. Walle, F. Corbin, R Boucheron, and D. Fréchou. Size measurement of bubbles in a cavitation tunnel by digital in-line holography. *Appl. Opt.*, 50:H1–H9, 2011.

[59] T. T. E. Yeo, S. H. Ong, Jayasooriah, and R. Sinniah. Autofocusing for tissue microscopy. *Image Vision Comput.*, 11:629–639, 1993.

[60] Karl K Pingle. Visual perception by a computer. *Automatic interpretation and classification of images*, pages 277–284, 1969.

[61] Per-Erik Danielsson. History and definition of the sobel operator by irwin sobel february 2, 2014, 2014.

[62] Francois Bruno, Jean-Baptiste Laudereau, Max Lesaffre, Nicolas Verrier, and Michael Atlan. Phase-sensitive narrowband heterodyne holography. *Appl. Opt.*, 53(7):1252–1257, Mar 2014.

[63] R. L. Powell and K. A. Stetson. Interferometric vibration analysis by wavefront reconstruction. *J. Opt. Soc. Am.*, 55:1593, 1965.

[64] C. C. Aleksoff. Temporally modulated holography. *Applied Optics*, 10:1329–1341, 1971.

[65] Pascal Picart, Eric Moisson, and Denis Mounier. Twin-sensitivity measurement by spatial multiplexing of digitally recorded holograms. *Applied Optics*, 42(11):1947–1957, 2003.

[66] Dan N Borza. Mechanical vibration measurement by high-resolution time-averaged digital holography. *Measurement Science and Technology*, 16(9):1853, 2005.

[67] Giancarlo Pedrini, Wolfgang Osten, and Mikhail E. Gusev. High-speed digital holographic interferometry for vibration measurement. *Appl. Opt.*, 45(15):3456–3462, May 2006.

[68] Francois Bruno, Jerome Laurent, Daniel Royer, and Michael Atlan. Holographic imaging of surface acoustic waves. *Applied Physics Letters*, 104(8):–, 2014.

[69] Lin Cong, Wen Xiao, Lu Rong, Feng Pan, Jianyi Li, Fanjing Wang, and Zhaohai Zhang. Long distance real-time measurement of multi-points micro-vibration in region by digital holography. *Optik-International Journal for Light and Electron Optics*, 2014.

[70] B. Samson and M. Atlan. Short-time fourier transform laser doppler holography. *Journal of the European Optical Society - Rapid publications*, 8(0), 2013.

[71] M. Atlan, M. Gross, T. Vitalis, A. Rancillac, B. C. Forget, and A. K. Dunn. Frequency-domain, wide-field laser doppler in vivo imaging. *Optics Letters*, 31(18):2762–2764, 2006.

[72] G. Pedrini and H. J. Tiziani. Short-coherence digital microscopy by use of a lensless holographic imaging system. *Applied Optics*, 41:4489–4496, August 2002.

[73] Nicolas Verrier, Daniel Alexandre, and Michel Gross. Laser doppler holographic microscopy in transmission: application to fish embryo imaging. *Opt. Express*, 22(8):9368–9379, Apr 2014.

[74] M. Simonutti, M. Paques, J. A. Sahel, M. Gross, B. Samson, C. Magnain, and M. Atlan. Holographic laser doppler ophthalmoscopy. *Opt. Lett.*, 35(12):1941–1943, 2010.

[75] W. Xu, MH Jericho, HJ Kreuzer, and IA Meinertzhagen. Tracking particles in four dimensions with in-line holographic microscopy. *Optics Letters*, 28(3):164–166, 2003.

[76] P. Marquet, B. Rappaz, P. J. Magistretti, E. Cuche, Y. Emery, T. Colomb, and C. Depeursinge. Digital

holographic microscopy: a noninvasive contrast imaging technique allowing quantitative visualization of living cells with subwavelength axial accuracy. *Optics Letters*, 30:468–470, March 2005.

[77] Jorge Garcia-Sucerquia, Wenbo Xu, Stephan K. Jericho, Peter Klages, Manfred H. Jericho, and H. Jürgen Kreuzer. Digital in-line holographic microscopy. *Appl. Opt.*, 45(5):836–850, 2006.

[78] J. Sheng, E. Malkiel, and J. Katz. Digital holographic microscope for measuring three-dimensional particle distributions and motions. *Applied Optics*, 45:3893–3901, June 2006.

[79] Michael Atlan, Michel Gross, Pierre Desbiolles, Émilie Absil, Gilles Tessier, and Maïté Coppey-Moisan. Heterodyne holographic microscopy of gold particles. *Optics Letters.*, 33(5):500–502, 2008.

[80] Michael Atlan, Pierre Desbiolles, Michel Gross, and Maïté Coppey-Moisan. Parallel heterodyne detection of dynamic light-scattering spectra from gold nanoparticles diffusing in viscous fluids. *Opt. Lett.*, 35(5):787–789, 2010.